

Research on the Application of Surface Wave Method for the Precise Detection of Shallow Coal Seam Mined-Out Area and Overburden

Yu Li

Chang'an University <https://orcid.org/0000-0002-1636-5683>

Zhi Yang

Chang'an University

Guangui Zou (✉ cumtzgg@foxmail.com)

<https://orcid.org/0000-0002-4423-2335>

Fei Zhao

The institute of geophysical and chemistry exploration of Shanxi

Yan Liu

Chang'an University

Case study

Keywords: Shallow coal mined-out area, overburden, MASW, low-frequency focus factor, phase-shift method, dispersion energy, shear wave velocity

Posted Date: February 8th, 2022

DOI: <https://doi.org/10.21203/rs.3.rs-1302235/v1>

License:   This work is licensed under a Creative Commons Attribution 4.0 International License.

[Read Full License](#)

1 Research on the application of surface wave method for the precise detection
2 of shallow coal seam mined-out area and overburden

3 Yu Li^{1,2}, Yang zhi^{1,2}, Guangui Zou^{3,4}, Fei Zhao⁵, Yan Liu^{1,2}

4 ¹School of Geological Engineering and Geomatics, Chang'an University, Xi'an, 710054, China;

5 ²Key Laboratory of Western China Mineral Resources and Geological Engineering, Chang'an
6 University, Xi'an 710054, China;

7 ³State Key Laboratory of Coal Resource and Safety Mining, China University of Mining and
8 Technology (Beijing), Beijing 100083, China;

9 ⁴College of Geoscience and Surveying Engineering, China University of Mining and
10 Technology (Beijing), Beijing 100083, China;

11 ⁵The institute of geophysical and chemistry exploration of Shanxi, Yuncheng 044000, China.

12 **Corresponding author:** Guangui Zou; **E-mail:** cumtzzg@foxmail.com.

13 **ABSTRACT**

14 To finely detect the boundary of a shallow coal mined-out area, as well as the extent of
15 the overburden affected by the mined-out area, and to analyze the factors and interrelationships
16 between the detection depth and lateral resolution of the multichannel analysis of surface waves
17 (MASW) method, a low-frequency focusing factor is introduced into the phase-shift method, and
18 a low-frequency focusing phase-shift method is proposed to improve the detection depth and
19 lateral resolution of the MASW method. The method is applied to the processing and analysis of
20 measured active-source surface waves. The results show that the low-frequency focused phase-
21 shift method has the significant advantage of extracting the dispersion energy at low-frequency
22 side from the short receiver spread. The receiver-spread length of the measured data used to
23 calculate the dispersion energy is 35 m, which meets the 70 m detection depth of the target coal
24 mined-out area. The measured data were processed to obtain high-precision horizontal slices of
25 the shear wave velocity along the coal seam and in the overburden at different depths. The

26 former clearly identify the boundaries of the coal mined-out areas and the locations and
27 geometries of the security coal pillars and estimate the main coal mining direction to be
28 approximately 23° NW, which is in general agreement with the actual direction of 21° NW of the
29 back workings in the mining area of the study site. One mined-out area of approximately 30 m in
30 width, one mined-out area greater than 50 m in width, and one roadway of approximately 10 m
31 in width are inferred. The latter directly shows the extent of the overburden affected by the coal
32 mined-out area gradually decreasing as the depth becomes shallower. The severe influence
33 extent on the surface is delineated and mutually supported by the surface cracks in the village
34 east of the research site. The effectiveness of the low-frequency focused phase-shift method in
35 improving the depth and lateral resolution of the MASW method and the feasibility of the
36 MASW method in precise detection of shallow coal mined-out area and overburden are
37 confirmed.

38 **KEYWORDS:** Shallow coal mined-out area; overburden, MASW; low-frequency focus factor;
39 phase-shift method; dispersion energy; shear wave velocity

40 1. INTRODUCTION

41 Coal resources are the main energy source in China. Long-term, high-intensity coal mining
42 has formed large mined-out areas, causing safety problems such as gas enrichment and water
43 accumulation and posing a severe threat to safe coal mine production (Liu et al. 2005). Shallow
44 coal mined-out area can also cause surface subsidence and collapse, significantly affecting the
45 safety of the large buildings and the environment. In recent years, the coal “de-capacity” policy
46 has led to the accelerated closure of many resource-depleted and “backward capacity” (plants
47 with low capacity or inadequate equipment) mines, resulting in a large number of

48 closed/abandoned mines. These closed or abandoned mines still contain large amounts of
49 available resources, such as coalbed methane (Yuan et al. 2018; Wang et al. 2021). Therefore, the
50 precise detection of the boundary of the mined-out area, the location and scale of the security
51 coal pillars, and the extent of the overburden affected by the mined-out area are of great
52 significance to the safe production of coal mines, the planning and utilization of surface land in
53 the mining area and the development of surface coalbed methane.

54 According to the differences in physical properties such as elasticity or electricity between
55 mined-out area and surrounding rock, geophysical exploration is used to detect and to identify
56 mined-out area. The mainstream methods are mainly divided into seismic methods (Yang et al.
57 2004; Cheng et al. 2008; Li et al. 2017; Zhang et al. 2021) and electromagnetic methods (Cheng
58 et al. 2010; Yang 2012; Mu 2018; Xue et al. 2018; Wang et al. 2019; Su et al. 2020; Chen et al.
59 2021); these methods have achieved good results in some application cases. There are many
60 geophysical exploration methods that should be selected according to the geological conditions
61 and characteristics of the coal mined-out area to achieve positive results (Fu 2014; Li 2017).
62 Shallow coal mined-out area generally refers to coal seams buried at a depth of 50-150 m.
63 Seismic reflection waves often overlap with high-energy first arrivals and surface waves in the
64 time window, forming strong interference. Because of the shallow depth of the coal seam, using
65 surface waves in seismic data provides favorable conditions and possibilities for detection in the
66 mined-out area. There is relatively little research work on overburden detection in coal mined-
67 out area because of the difficulty in effectively detecting the extent of overburden deformation
68 and damage due to the slight changes in physical characteristics (Cheng et al. 2000; Cheng 2008;
69 Zhang et al. 2009). With the development of fine data processing technology and geophysical
70 exploration equipment, four-dimensional seismic, time-shifted resistivity, time-shifted geological

71 radar, and time-shifted high-density resistivity methods have been applied in overburden
72 detection and have achieved better results (Du et al. 2014; Li et al. 2019; Yuan et al. 2021).
73 Compared with time-shifted observation techniques, multichannel analysis of surface waves
74 (MASW) has a good response to the reduction of shear wave velocity caused by the overburden
75 deformation and damage, and has the advantages of economy and efficiency.

76 The application and research of the surface wave method in engineering geology surveys in
77 China started early. The application results show the feasibility of the method in detecting old
78 mined-out areas (Yu et al. 1996). Liu et al. (1996) used the SWS model transient surface wave
79 multichannel data acquisition and processing system developed in China to detect an old kiln in
80 the Antaibao open-pit mine and interpreted the location of the old kiln based on the one-
81 dimensional surface wave apparent velocity curves. They verified the results by drilling. Chang
82 et al. (2002) explored the MASW method based on the relationship between the geophysical
83 characteristics of the mined-out area and the response of Rayleigh wave. The profile showed a
84 significant decrease in shear wave velocity within the mined-out area, and the boundary of the
85 mined-out area was clear. Wang et al. (2004) used the high-energy Rayleigh wave to interpret the
86 mined-out area based on the difference in Rayleigh wave velocity between the fallout area and
87 the coal pillar above the mined area. Chen et al. (2010) analyzed the Rayleigh wave propagation
88 characteristics in the mined-out area and the key technologies for detecting the mined-out area.
89 The example results were consistent with the pavement deformation and drilling results. Li (2012)
90 used the microtremor technique to detect mined-out area and inferred that low-velocity zone was
91 mined-out area and that high-velocity body was the residual coal pillar in the shear wave velocity
92 section. Rector et al. (2015) used surface wave tomography to detect mining voids in coal seams
93 and obtained the velocity and attenuation characteristics of Rayleigh wave within a depth of 5 m.

94 The results showed that the rock above the mining voids exhibited low velocity and that the
95 amplitude attenuation became large. Yan et al. (2019) applied the microtremor technique to
96 detect mined-out area using multiple triangle-mounted array and spatial autocorrelation method,
97 delineating the shallow mined-out area. The result matched the high-density resistivity method
98 and drilling results. The above research works have achieved good results and promotes the
99 development of surface wave methods to detect coal mined-out area. The main problems
100 currently faced can be broadly summarized into two aspects: first, the MASW has difficulty
101 reaching a detection depth of 50 m; second, the microtremor technique uses 2-D receiver array,
102 and the exploration point interval is often large, in addition to the absence of high-frequency
103 dispersion energy, which affects the detection accuracy of the mined-out area and the overburden.

104 In this paper, we improve the phase-shift method, shorten the receiver-spread length
105 calculated dispersive energy, promote the focus of dispersive energy at the low-frequency side,
106 and enhance the detection depth and lateral resolution of the MASW method. Finally, the
107 simulated data and the measured data of the shallow coal mined-out area are processed by using
108 the improved phase-shift method.

109 **2. LOW-FREQUENCY FOCUSING PHASE-SHIFT METHOD**

110 The implementation of the MASW method (Park et al. 1999) consists of three main steps: (1)
111 extraction of surface wave dispersion energy from seismic records; (2) detection of the extreme
112 values of the dispersion energy to obtain the dispersion curve; and (3) inversion of the dispersion
113 curve to obtain a 1D shear wave velocity profile. We construct the pseudo-2D shear wave
114 velocity section by merging multiple 1D shear wave velocity profiles. Each 1D velocity profile is
115 the integrated response of the stratigraphic structure below the receiver spread used to calculate

116 the dispersion energy, and increasing the receiver-spread length increases the lateral averaging
117 effect of the stratigraphic structure. However, increasing the receiver-spread length promotes the
118 extension of the dispersion energy to lower frequencies, which can obtain information from
119 greater depths. Therefore, the receiver-spread length for calculating the dispersive energy in step
120 1 affects the lateral resolution and detection depth of the MASW method.

121 2.1 Phase-shift method

122 The phase-shift method was proposed by Park et al. in 1998 to extract the surface wave
123 dispersion energy. This method has the advantages of adapting to unequal spacing receiver
124 spread, low computational effort, and good extraction of the dispersion energy of the
125 fundamental mode. Surface wave dispersion analysis requires converting a seismic record in the
126 time-space (t - x) domain into a dispersive energy image in the frequency-phase velocity (f - v)
127 domain. Assuming that $U(x,t)$ is the shot record, the spectrum $U(x,\omega)$ can be written as the
128 product of the amplitude spectrum and the phase spectrum in the form of a one-dimensional
129 Fourier transform along the direction of time t

$$130 \quad U(x, \omega) = A(x, \omega)P(x, \omega) \quad (1)$$

131 where $A(x,\omega)$ is the amplitude spectrum and $P(x,\omega)$ is the phase spectrum.

132 In equation (1), each frequency component of the surface wave is separated, and its travel
133 time information is contained in the phase spectrum. The dispersion information is contained in
134 the phase spectrum $P(x,\omega)$. The amplitude spectrum contains information on spherical diffusion,
135 amplitude attenuation, etc. The phase is expressed in exponential form, and the spectrum is
136 written as

$$137 \quad U(x, \omega) = e^{-i\Phi x} A(x, \omega) \quad (2)$$

138
$$\Phi = \omega/V_\omega$$

139 where Φ is the phase difference; ω is the angular frequency; V_ω is the phase velocity
140 corresponding to the frequency component ω ; and x is the shot-receiver distance.

141 Amplitude normalization in the x -direction due to the effect of spherical diffusion and
142 attenuation on amplitude. Then, the integration of equation (2) is made as follows

143
$$V(\varphi, \omega) = \int e^{-i(\Phi-\varphi)x} \left[\frac{A(x, \omega)}{|A(x, \omega)|} \right] dx \quad (3)$$

144 Equation (3) can be interpreted as the summing of the wavefield at a given frequency after
145 its phase shift φ along the x -direction. For a given frequency ω , if the scanned phase φ is equal to
146 Φ , i.e.,

147
$$\varphi = \Phi = \frac{\omega}{V_\omega} \quad (4)$$

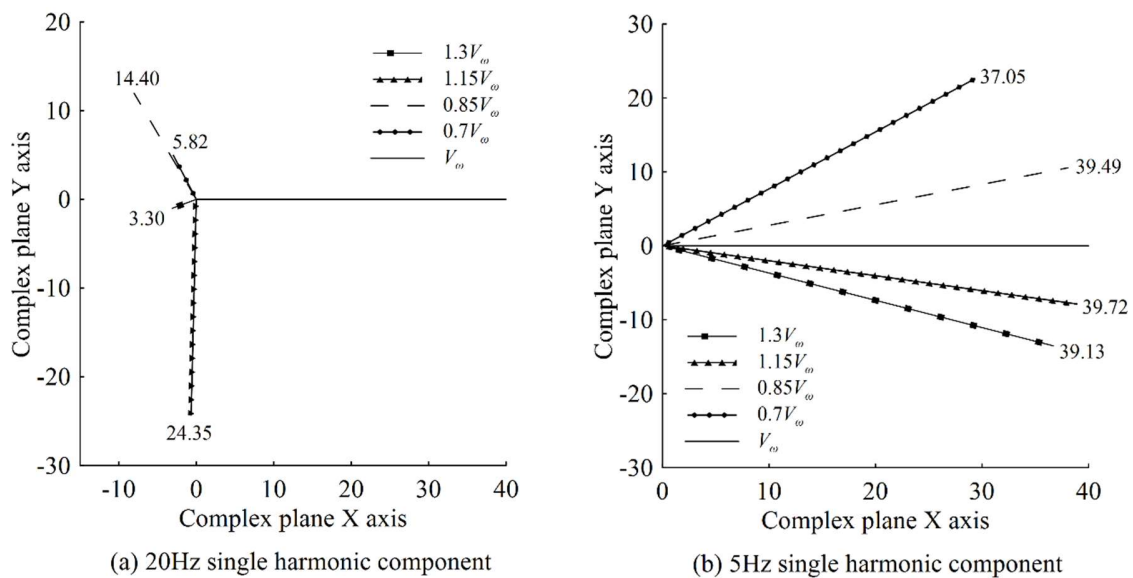
148 then the integration result $|V(\varphi, \omega)|$ would be the maximum value.

149 Converting the phase φ to phase velocity V_ω according to equation (4), from $f=\omega/2\pi$, the
150 final f - v domain dispersion energy image can be obtained. $|V(\varphi, \omega)|$ represents the dispersion
151 energy value. The dispersion curve is obtained by detecting the extreme values of the dispersion
152 energy.

153 2.2 Dispersion energy focusing factor

154 The phase information Φx in equation (3) represents the amount of phase change that occurs
155 as the surface wave propagates to the shot-receiver distance x . $\Phi-\varphi$ represents the error between
156 the scanned phase and the true phase. Based on a linear recording geometry with 1 m receiver
157 spacing and 40 receivers, the shot-receiver distance x is 39 m. Keeping x constant, the effect of
158 parameters Φ and φ on the focus of dispersion energy are analyzed. Land seismic surface waves

159 generally conform to positive dispersion characteristics; i.e., the high-frequency Φ value is small,
 160 and the low-frequency Φ value is large. Consider two surface wave single-frequency
 161 components at a high frequency of 20 Hz and low frequency of 5 Hz, given Φ values of $\pi/5$ and
 162 $\pi/40$, respectively. If $\Phi=\varphi$, the scan phase is in the correct phase, the complex numbers of the
 163 two single-frequency components are in the same direction and the positive direction of the x -
 164 axis, and the dispersion energy $|V(\varphi, \omega)|$ is calculated using equation (3) with the maximum
 165 value of 40. If the scan phase φ is large or small, $|V(\varphi, \omega)|$ would be smaller than the maximum
 166 value, as shown in Figure 1.



167 (a) 20Hz single harmonic component
 168 (b) 5Hz single harmonic component
 169 **Fig.1** Comparative analysis of dispersion energy of single frequency components

169 The error of the scanned phase φ is converted to the error of the phase velocity V_ω using
 170 equation (2), and four error cases are considered where the scanned phase velocity is 70%, 85%,
 171 115%, and 130% of the true phase velocity V_ω . The 20 Hz single-frequency component yields
 172 $|V(\varphi, \omega)|$ value of 5.82, 14.40, 24.35, and 3.30, respectively, which are different from the
 173 maximum value of 40, with large errors. The range of the error is -15.65~36.70. The 5 Hz
 174 single-frequency components yield $|V(\varphi, \omega)|$ values of 37.05, 39.49, 39.72, 39.13, respectively,

175 which are closer to the maximum value of 40, and the error range is only -0.28 ~ -2.95. The
 176 detailed errors are shown in Table 1.

177 **Table1** $|V(\varphi, \omega)|$ varies with frequency

Frequency	$ V(\varphi, \omega) $				
	$0.7V_\omega$	$0.85V_\omega$	V_ω	$1.15V_\omega$	$1.3V_\omega$
20Hz	5.82	14.40	40	24.35	3.30
	-34.18	-25.60		-15.65	-36.70
5Hz	37.05	39.49	40	39.72	39.13
	-2.95	-0.51		-0.28	-0.87

178 To improve the focus of the 5 Hz single-frequency component dispersive energy, the most
 179 effective way is increasing the shot-receiver distance x and expanding the total phase difference.
 180 The number of receives is increased from 40 to 120, and $|V(\varphi, \omega)|$ is increased linearly from 40
 181 to 120 in the absence of errors, while the recording geometry and other parameters are kept
 182 constant. In the four error cases, $|V(\varphi, \omega)|$ is 53.54, 106.64, 112.59, and 97.71, respectively,
 183 compared to the maximum value of 120, with an error range of -7.41 to -66.46; the detailed
 184 errors are shown in Table 2. The results show that increasing the shot-receiver length leads to
 185 $|V(\varphi, \omega)|$ changes at a faster rate, so enhances the focus of the dispersion energy.

186 **Table2** $|V(\varphi, \omega)|$ varies with the number of receivers

Frequency	Number of Receivers	$ V(\varphi, \omega) $				
		$0.7V_\omega$	$0.85V_\omega$	V_ω	$1.15V_\omega$	$1.3V_\omega$
5Hz	40-channels	37.05	39.49	40	39.72	39.13
		-2.95	-0.51		-0.28	-0.87
	120-channels	53.54	106.64	120	112.59	97.71
		-66.46	-13.36		-7.41	-22.29

187 Improving the focus of the dispersion energy at low frequencies by increasing x reduces the
 188 lateral resolution of the MASW method. The study and improvement of the focus of the
 189 dispersion energy at the low-frequency side while keeping x constant have important practical

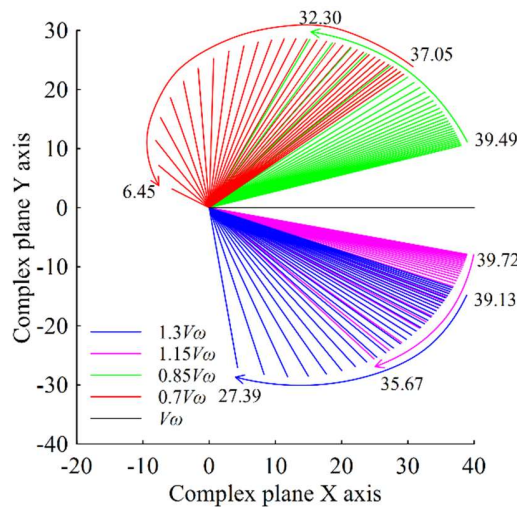
190 application value. By adding a positive phase factor τ to the phase component $e^{-i(\phi-\varphi)x}$ of
 191 equation (3), we can rewrite equation (1) as

$$192 \quad V'(\varphi, \omega) = \int e^{-i(\phi+\tau-\varphi)x} \left[\frac{A(x, \omega)}{|A(x, \omega)|} \right] dx \quad (5)$$

$$193 \quad \tau = \omega/v^*$$

194 where τ is the focusing factor; v^* is the reference phase velocity.

195 Figure 2 clearly shows the dynamic decreasing trend and rate of change in $|V(\varphi, \omega)|$ as the
 196 focus factor τ increases from 0 to $3\pi/40$; the larger the phase velocity error is, the faster the
 197 decrease in $|V(\varphi, \omega)|$. The final values of $|V(\varphi, \omega)|$ for the four error cases are 6.45, 32.30,
 198 35.67, and 27.39, with errors ranging from -4.33 to -33.55; the detailed errors are shown in Table
 199 3.



200

201 **Fig.2** Dynamic variation of dispersion energy with focus factor

202

Table3 $|V(\varphi, \omega)|$ varies with focus factor

Frequency	Focus factor	$ V(\varphi, \omega) $				
		$0.7V_\omega$	$0.85V_\omega$	V_ω	$1.15V_\omega$	$1.3V_\omega$
5Hz	$\tau = 0$	37.05	39.49	40	39.72	39.13
		-2.95	-0.51		-0.28	-0.83
	$\tau = \frac{3\pi}{40}$	6.45	32.30	40	35.67	27.39
		-33.55	-7.70		-4.33	-12.61

203 The focus factor τ is introduced in the phase-shift method to improve the focus of the
204 dispersion energy at the low-frequency side, where $|V'(\varphi, \omega)|$ and V'_ω called the low-frequency
205 focused dispersion energy and low-frequency focused phase velocity respectively. The focus
206 factor needs to be chosen reasonably according to the reference phase velocity in the real data.
207 The reference phase velocity should consider both the total phase variation at low frequency and
208 avoid spatial aliasing at high frequency. It is recommended to take values 1~2 times surface
209 wave group velocity. From equation (5), a dispersion energy image of the low-frequency focused
210 mode can be obtained in the f - v' domain, and the true phase velocity V_ω corresponding to the
211 frequency component ω can be calculated according to equation (6).

$$212 \quad V_\omega = \frac{\omega}{\Phi - \tau} = \frac{\omega}{\omega/V'_\omega - \tau} \quad (6)$$

213 The low-frequency focused phase-shift method enhances the focus of the dispersion energy
214 at low-frequency side without increasing the receiver-spread length of calculated dispersive
215 energy in the MASW method, increasing the detection depth while providing a significant
216 improvement to the lateral resolution of the MASW method.

217 3. NUMERICAL SIMULATION

218 Numerical simulation of seismic wavefields is an important research tool in seismic
219 exploration. For a two-dimensional isotropic medium, the first-order velocity-stress elastic wave
220 equation for Rayleigh wave satisfying Hooke's law (Virieux 1984; 1986) is

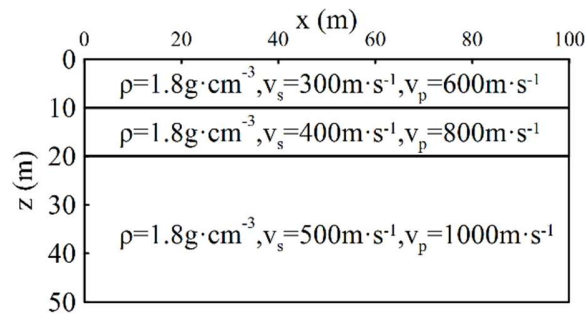
$$\left\{ \begin{array}{l}
 \rho(x, z) \frac{\partial v_x(x, z, t)}{\partial t} = \frac{\partial \sigma_{xx}(x, z, t)}{\partial x} + \frac{\partial \sigma_{xz}(x, z, t)}{\partial z} \\
 \rho(x, z) \frac{\partial v_z(x, z, t)}{\partial t} = \frac{\partial \sigma_{xz}(x, z, t)}{\partial x} + \frac{\partial \sigma_{zz}(x, z, t)}{\partial z} + \varphi(x, z, t) \\
 \rho(x, z) \frac{\partial \sigma_{xx}(x, z, t)}{\partial t} = (\lambda(x, z) + 2\mu(x, z)) \frac{\partial v_x(x, z, t)}{\partial x} + \lambda(x, z) \frac{\partial v_z(x, z, t)}{\partial z} \\
 \rho(x, z) \frac{\partial \sigma_{zz}(x, z, t)}{\partial t} = \lambda(x, z) \frac{\partial v_x(x, z, t)}{\partial x} + (\lambda(x, z) + 2\mu(x, z)) \frac{\partial v_z(x, z, t)}{\partial z} \\
 \rho(x, z) \frac{\partial \sigma_{xz}(x, z, t)}{\partial t} = \mu(x, z) \left(\frac{\partial v_x(x, z, t)}{\partial x} + \frac{\partial v_z(x, z, t)}{\partial z} \right)
 \end{array} \right. \quad (7)$$

221 where $\sigma_{xx}(x, z, t)$, $\sigma_{xz}(x, z, t)$ and $\sigma_{zz}(x, z, t)$ are the three components of the in-plane stress;
 222 $v_x(x, z, t)$ and $v_z(x, z, t)$ are the horizontal and vertical components of velocity, respectively;
 223 $\lambda(x, z)$ and $\mu(x, z)$ are Lamé constants; $\rho(x, z)$ is the density; and $\varphi(x, z, t)$ is the seismic source
 224 term.
 225

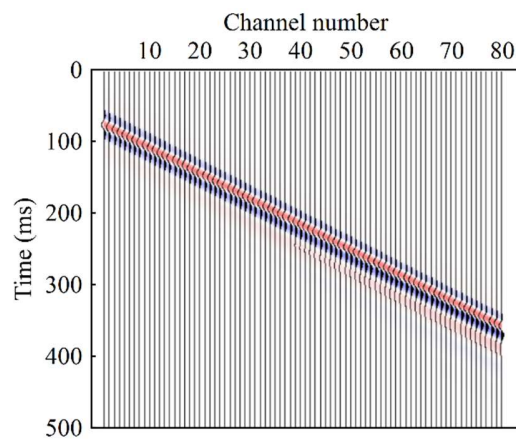
226 The source is placed on the surface, and the vertical source is simulated by loading the
 227 source term onto the $v_z(x, z, t)$. A transversely isotropic medium replacement method is used to
 228 achieve a free boundary at the upper part of the model. A biaxial perfectly matched layer
 229 technique is used to address the boundary reflection problems (Yan 2019).

230 A 3-layer horizontal layered model is established to verify the effect of the low-frequency
 231 focused phase-shift method to enhance the dispersive energy at the low-frequency side, as shown
 232 in Figure 3. Density keeps constant at 1 800 kg/m³ in the model, the thickness of the first layer is
 233 set to 10 m, with a compressional wave velocity of 600 m/s and shear wave velocity of 300 m/s;
 234 the thickness of the second layer is set to 10 m, with a compressional wave velocity of 800 m/s
 235 and shear wave velocity of 400 m/s; the third layer is semi-infinite space, with a compressional
 236 wave velocity of 1000 m/s and shear wave velocity of 500 m/s. The differential grid is 401 × 201,
 237 and the grid step size is $\Delta x = \Delta z = 0.25$ m. The source is located at (10, 0) on the surface, and a
 238 Ricker wavelet with a dominant frequency of 30 Hz is selected. The seismic recording sampling
 239 rate is 0.5 ms and the recording duration is 0.5 s. Eighty receivers are placed on the surface, with

240 a receiver spacing of 1 m and a minimum offset of 10 m. The wave equation is solved using
 241 staggered-grid finite difference method with the second-order difference in time and tenth-order
 242 difference in space. The theoretical seismic record is shown in Figure 4.



243

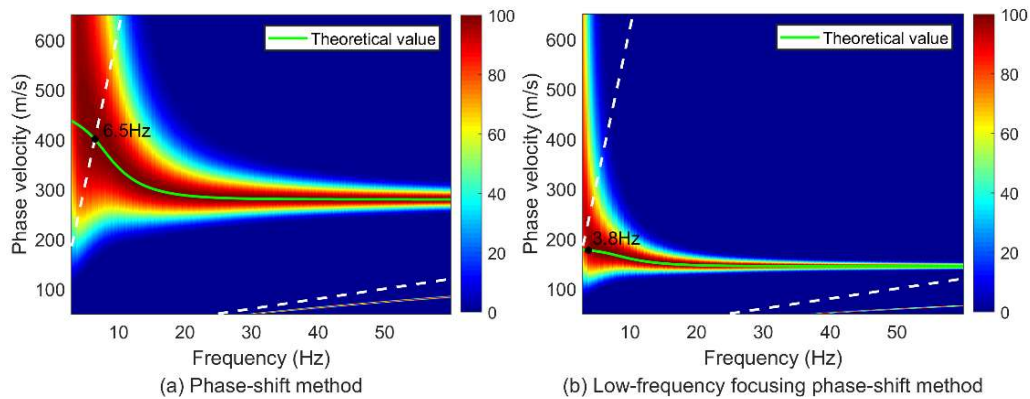
244 **Fig.3** Three-layer model

245

246 **Fig.4** Theoretical seismic record

247 The surface wave energy in the seismic record is overwhelmingly dominant, showing
 248 linearity and dispersion characteristics, with a group velocity of approximately 300 m/s; the body
 249 wave energy is weak, and no continuous event is observed. The phase velocity range is set to 50
 250 to 650 m/s with a velocity increment of 1 m/s, and the frequency range is 3 to 60 Hz with a
 251 frequency increment of 0.1 Hz. The first 32 channels are intercepted, and the dispersion energy is
 252 extracted using the phase-shift method and the low-frequency focused phase-shift method; as
 253 shown in Figure 5, the reference phase velocity for the latter is the surface wave group velocity.

254 According to the spatial sampling principle, the two white dashed lines in Figure 5 determine the
 255 reliable range of surface wave dispersion energy. The points on the left white dashed line is
 256 determined by formula $f/v=1/2L$ (L is the receiver-spread length) and the points on the right
 257 white dashed line is determined by formula $f/v=1/2dx$ (dx is the receiver spacing).



258

259 **Fig.5** Dispersion energy images

260 As shown in Figure 5(a), for the dispersion energy extracted by the phase-shift method, the
 261 theoretical phase velocity value shown green line coincides with the trend of the peak dispersion
 262 energy; the limiting wavelength determined by the receiver-spread length is 62 m, corresponding
 263 to a frequency of 6.5 Hz. As shown in Figure 5(b), for the dispersive energy extracted by the
 264 low-frequency focused phase-shift method, the low-frequency focused phase velocity value
 265 obtained by converting the theoretical phase velocity value from equation (6) coincides with the
 266 peak dispersive energy; the reliable minimum frequency determined from the dispersion energy
 267 is 3.8 Hz, which corresponds to a phase velocity V'_ω of 177 m/s. Then the low-frequency focused
 268 phase velocity is inverse converted and the phase velocity V_ω corresponding to 3.8 Hz is 431 m/s;
 269 the maximum wavelength reaches 113.4 m. The focus of the dispersive energy extracted by the
 270 low-frequency focused phase-shift method is generally better than that of the phase-shift method
 271 with the low frequency dropping from 6.5 Hz to 3.8 Hz, significantly increasing the detection
 272 depth with the same receiver-spread length.

273 4. EXAMPLE ANALYSIS

274 4.1 Overview of the study site

275 The study site is southwest of the Gushuyuan Mine of the Jincheng Anthracite Mining
276 Group, the surface is covered with loess, and the topographic changes are relatively small. The
277 coal-bearing strata are Carboniferous and Permian, and the #3 coal, #9 coal, and #15 coal are
278 stable recoverable coal seams. The target of this exploration is the mining area of the #3 coal
279 seam. The #3 coal seam is located in the lower part of the Shanxi Group, approximately 26.5 m
280 down from the K5 tuff and approximately 50 m from the #9 coal seam. The thickness of the coal
281 seam ranges from 2.81 to 7.67, with an average value of about 5.73m. Its direct top plate is
282 mostly gray–black sandy mudstone or siltstone, the old top is mostly gray thick-bedded
283 sandstone, and the bottom plate is generally gray–black siltstone or carbonaceous mudstone. The
284 #3 coal seam of the study site was mined in 1962, and the extent of the mined-out areas are
285 unknown because of the long mining timespan and the lack of primary geological data.

286 The study site is narrow, with a length of 140*70 m. An adjacent borehole reveals that
287 the depth of coal seam #3 in the site is approximately 60~70 m. At present, this site is densely
288 populated with buildings, limiting observation line layout. In addition, there are high-voltage
289 transmission lines in the site and close to major traffic roads, so strong electromagnetic and
290 vibration noises are present, which have a serious impact on the quality of seismic data.

291 4.2 Data acquisition

292 To precisely identify the range of the mined-out area, the security coal pillar, and the
293 influence extent of the overburden in the mined-out site, multiple 2D parallel observation lines

294 were laid out for high-density data acquisition. According to the site-building location pattern,
295 six parallel observation lines (L1~L6) were laid, with an orientation of 75° N.E., and each line
296 length was 140m and evenly distributed at the site, as shown in Figure 6.

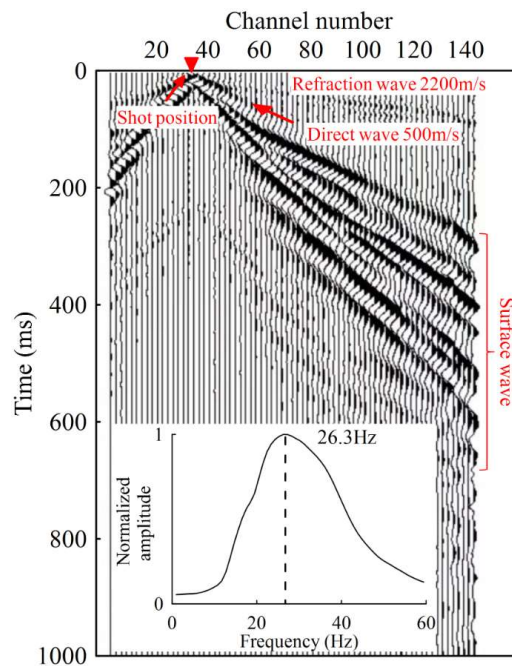


297
298 **Fig.6** Study site and parallel lines layout

299 The seismic data acquisition equipment is an ARIES digital seismograph equipped with a
300 10Hz natural frequency geophone. The receiver spacing should be minimized to improve the
301 identification of the mined-out area for this data acquisition. Because of the short observation
302 line, the recording geometry adopts a fixed receiver spread of 141 channels, with a source
303 spacing of 2 m and a receiver spacing of 1 m. Since the detection depth needs to reach 65 m, a
304 dynamic energy drop weigh with 400 kg hammer is selected for the source and hammer lift
305 height is 2.6m. This is conducive to noise suppression and generating low-frequency surface
306 waves to enhance signal-to-noise ratio of surface waves while improving the detection depth of
307 the MASW method.

308 The seismic data sampling rate is 1 ms, and the recording length is 1 s. One original seismic
309 record of the L2 line is shown in Figure 7, and the shot point is located at channel number 38
310 (marked by a red triangle). The surface wave energy in the seismic record is overwhelmingly

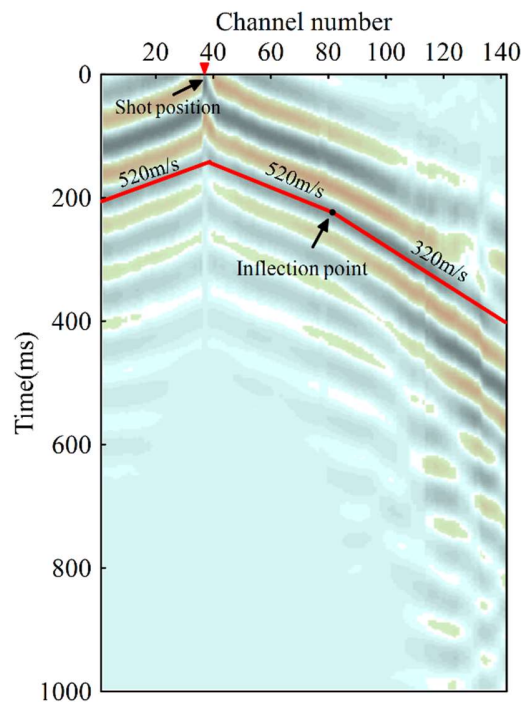
311 dominant, showing linearity and apparent dispersion characteristics. The amplitude spectrum
 312 shows that the bandwidth of the surface wave is 3~60 Hz, the dominant frequency is 26.3 Hz,
 313 and the group velocity is 340 m/s. In addition to surface waves, direct waves and refracted waves
 314 can be identified in the seismic record, where the former has a velocity of approximately 500 m/s
 315 and the latter has a velocity of approximately 2200 m/s.



316
 317 **Fig.7** Original seismic record

318 The low frequency of the surface wave carries depth information; the seismic record of
 319 Figure 7 is low-pass filtered at 10 Hz and then displayed by variable density as shown in Figure
 320 8. There is a visible velocity inflection point in the linear event of the surface wave at channel
 321 number 82. The slope changes significantly, and the group velocities on the left and right sides of
 322 the inflection point are approximately 520 m/s and 320 m/s, respectively, by linear fitting. It is
 323 preliminary speculated that the low velocity characteristics of the deep medium to the right of the

324 velocity inflection point are related to the mined-out area, and the boundary of the mined-out
325 area need to be further determined on the horizontal slice of the shear wave velocity.



326

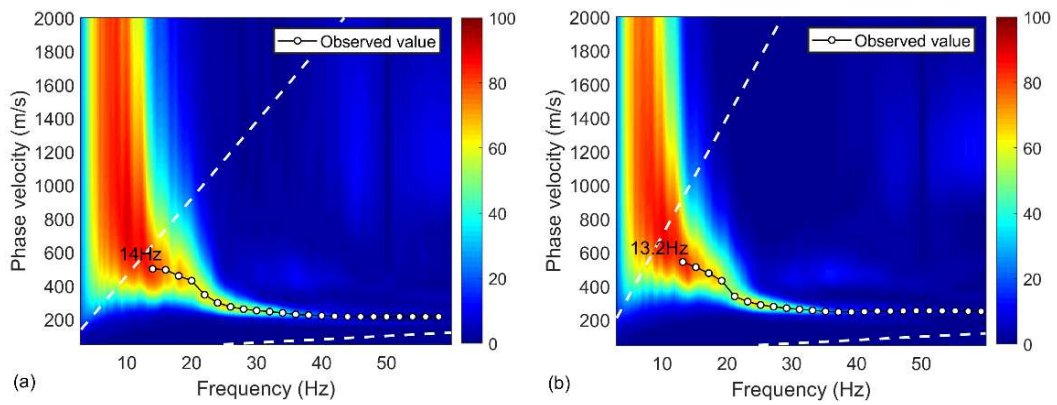
327 **Fig.8** Low-pass filtered seismic record

328 4.3 Data processing

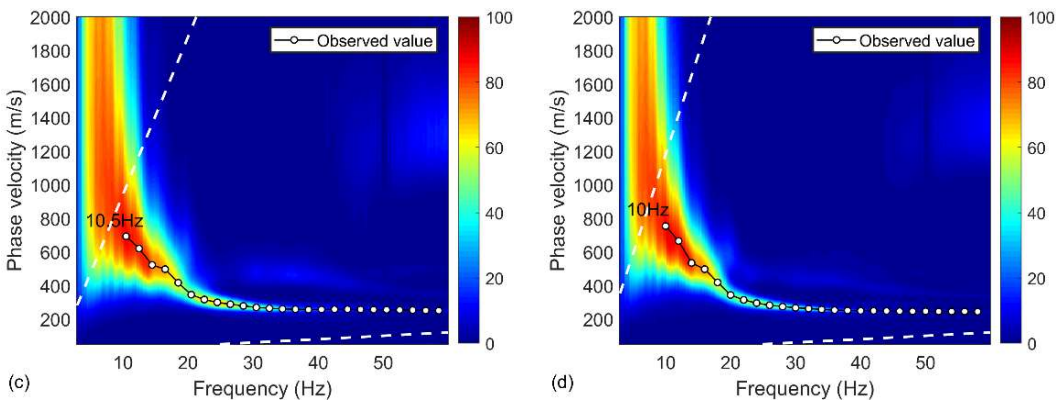
329 Data preprocessing has a significant influence on the results of the MASW method.
330 According to the principle of minimizing the surface wave field characteristics, combined with
331 the high signal-to-noise ratio of the surface waves in the original seismic record, the
332 preprocessing includes only 3~60Hz bandpass filtering, bad trace rejection and interpolation.
333 Receiver-spread length of the calculated dispersion energy directly affects the detection depth
334 and lateral resolution of the MASW method, and they are mutually constrained, so the receiver-
335 spread length need to be tested and selected in a compromise. Five receiver spreads of 24 (23 m),
336 36 (35 m), 48 (47 m), 60 (59 m), and 72 (71 m) channels are discussed below. We set the

337 velocity range from 50 m/s to 2000 m/s with a increment of 1 m/s, frequency range from 3 Hz to
 338 60 Hz with a increment of 0.1 Hz, and then use phase-shift method to extract the dispersive
 339 energy, which are shown in Figure 9a, b, c, d, and e, respectively.

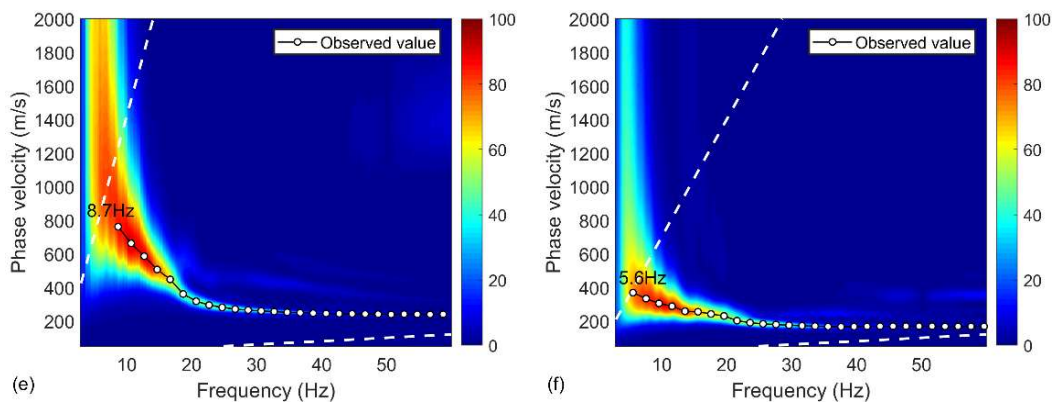
340



341



342



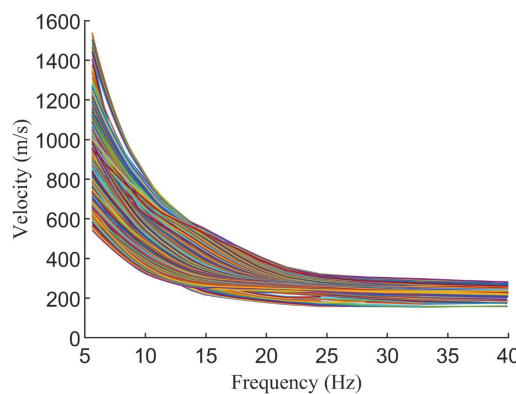
343 **Fig.9** Dispersion energy images

344 The dispersion energy in Figure 9 is mainly concentrated in the fundamental mode, with
345 little energy in the higher modes. In the dispersion energy images of the five receiver spreads, the
346 high-frequency sides are focused above 30 Hz and can reach 60 Hz. The focus of the dispersion
347 energy at low-frequency side is affected by the receiver-spread length, and the overall
348 performance is consistent with the above analysis; i.e., the longer the spread length is, the better
349 focus of the dispersion energy is at low-frequency side. According to the spatial sampling
350 principle and the focus of the dispersion energy, the minimum reliable frequencies for the five
351 receiver spreads are approximately 14 Hz, 13.2 Hz, 10.5 Hz, 10 Hz, and 8.7 Hz, and their
352 corresponding phase velocities are 501 m/s, 544 m/s, 693 m/s, 754 m/s, and 762 m/s. Based on
353 the half-wavelength criterion (Rix et al. 1991), the detection depths of these receiver spreads are
354 initially estimated to be 17.9 m, 20.6 m, 33.0 m, 37.7 m, and 43.8 m, none of which reach the 70
355 m detection depth of the target coal seam.

356 The 70 m detection depth of the target coal seam would be challenging to achieve by only
357 increasing the receiver-spread length. Additionally, an excessive increase in the receiver-spread
358 length would significantly reduce the lateral resolution of the MASW method, which would lead
359 to blurring the boundary of the mined-out area and even missing the identification of the mined-
360 out area in the 2D shear velocity section or horizontal slice. The low-frequency focused phase-
361 shift method is adopted based on a shorter receiver-spread length to improve the detection depth
362 and lateral resolution of the MASW method. The receiver spread with 36 channels is selected for
363 the low-frequency focused phase-shift method to extract the dispersion energy. The reference
364 phase velocity is set to 500 m/s, and the other calculation parameters are the same as those of the
365 phase-shift method; the dispersion energy is shown in Figure 9f. The focus of the dispersion
366 energy at low-frequency side is significantly improved, and the minimum reliable frequency is

367 reduced to 5.6 Hz, whose corresponding phase velocity V'_ω is 369 m/s and V_ω is 1408 m/s; the
368 estimated detection depth is 126 m, which comfortably reaches the 70 m detection depth of the
369 target coal seam.

370 During the dispersion energy calculation, the receiver spread is shifted forward by one
371 receiver spacing each observation line. Thus, a 1 m spacing one-dimensional shear wave
372 velocity profile can be obtained to strengthen the control of the coal mined-out area and
373 overburden. Six hundred six dispersion curves are extracted precisely from the six observation
374 lines (Figure 10), and the overall trend of the dispersion curves is similar, with a phase velocity
375 range of 160~1570 m/s.

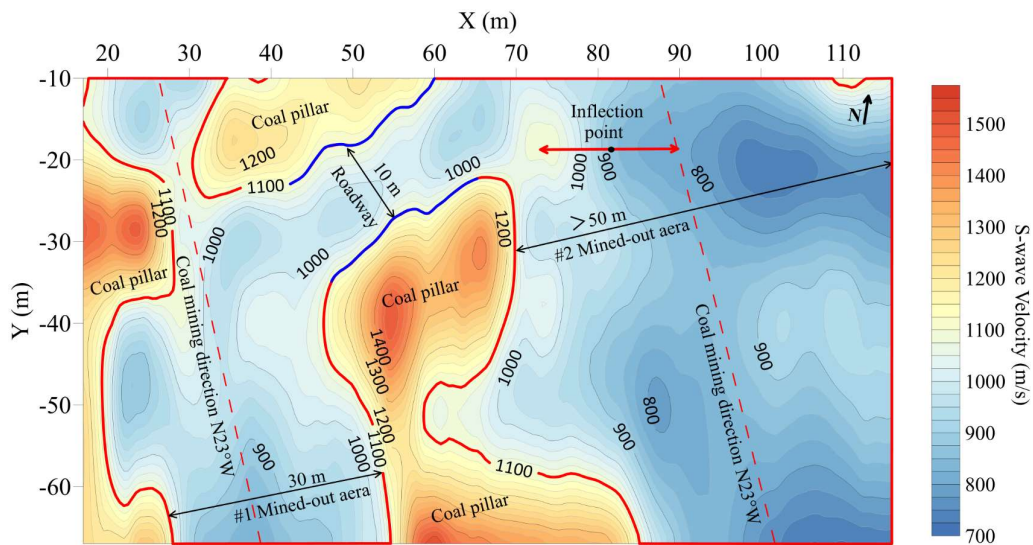


376

377 **Fig.10** Dispersion curve graph

378 The initial shear velocity model is established using the half-wavelength criterion, and the
379 damped least-squares method (Xia et al. 1999) is used to invert the shear velocity structure.
380 Figure 11 shows horizontal slices along the coal seam at 65 m depth with velocity ranging from
381 700 to 1600 m/s. The low-velocity zone and high-velocity zone in the horizontal slices have clear
382 boundaries and geometric features. The interpretation is based on the principle that the shear
383 wave in the coal mined-out area presents low velocity and the shear wave in the security coal
384 pillar offers high velocity, and also combined with the shear wave velocity range in the coal rock
385 physics experiment (Meng et al. 2006; Zhou 2012). The high-velocity zone with shear wave

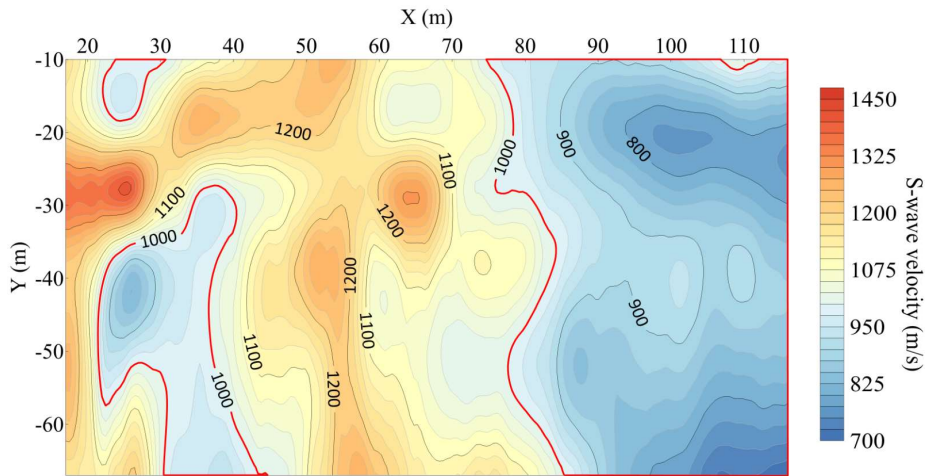
386 velocity more than 1 100 m/s in the horizontal slice can be interpreted as the security coal pillar,
 387 and the low-velocity zone less than 1 100 m/s is the mined-out area, as shown by red solid line.
 388 The width of the #1 mined-out area on the right side of the security coal pillar is approximately
 389 30 m, and the #2 mined-out area on the right side of the security coal pillar is not fully detected
 390 due to the small size of the study site. The current results show that its width is greater than 50 m.
 391 Based on the directional characteristics exhibited by the security coal pillars and the mined-out
 392 areas, this site's leading coal mining direction is estimated to be approximately 23° NW. This
 393 coincides with the actual direction of 21° NW for the layout of the recovery face in the mining
 394 area of the study site, thus supporting the reliability of the interpretation results. Additionally,
 395 one roadway with a width of approximately 10 m is interpreted as being approximately
 396 perpendicular to the direction of back mining, as shown by blue solid line. In addition, there is a
 397 visible inflection point of the surface wave group velocity in the seismic record in Figure 8,
 398 which is consistent with the result that the coal seam on the left side of the inflection point is
 399 partially mined and shows relatively high velocity. In contrast, the coal seam on the right side is
 400 wholly mined and indicates relatively low velocity.



401

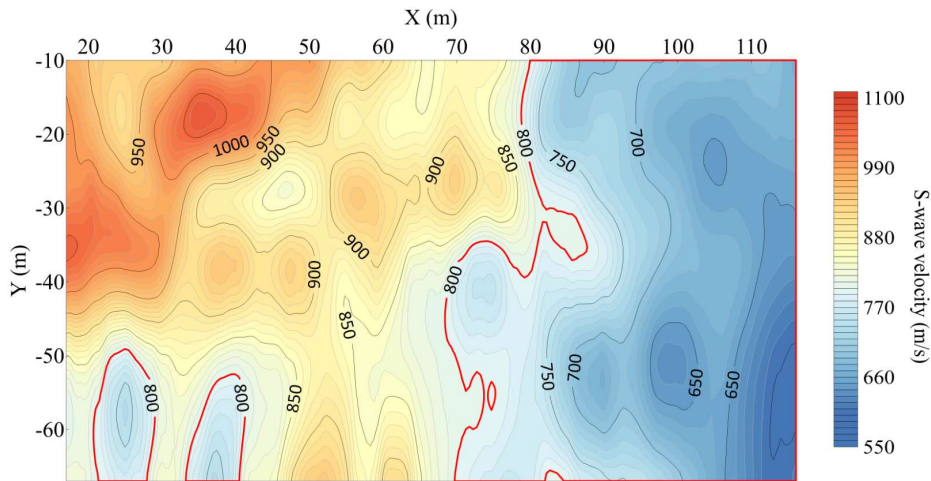
402 **Fig.11** Shear-wave horizontal slice along the coal seam (depth 65m)

403 After coal seam mining, the stress balance of the overburdens in the mined-out area is
404 disrupted, causing rock fracture, surface settlement, and cracking under the action of gravity. All
405 these consequences lead to a reduction in the shear wave velocity in the overburden. Figure 12
406 shows horizontal slices of the overburden at depths of 50 m, 35 m, 20 m, and 10 m. The extent of
407 the overburden affected by the mined-out area in the horizontal slice at a depth of 50 m (Figure
408 12a) is significant, shown by the red solid line. The morphology of the low-velocity zones is
409 basically the same as that of the low-velocity zones in the horizontal slice along the coal
410 seam (Figure 11), yet their extent has been reduced. As the depth decreases, the extent of
411 the low-velocity zones is gradually reduced. Because the width of the #1 mined-out area is
412 smaller, the influence on the overlying rock and soil layer is smaller. The influence extent of
413 the #1 mined-out area appears only in the southwest corner of the study site in the
414 horizontal slice at 35 m depth (Figure 12b). In the horizontal slice at 20 m depth (Figure
415 12c), the influence extent of the #1 mined-out area further decreases until it disappears in
416 the horizontal slice at 10 m depth (Figure 12d). In contrast, the width of the #2 mined-out
417 area is bigger, the influence on the overlying rock and soil layer is bigger. Although the
418 influence extent also generally decreases with depth, the extent of the low-velocity zones is
419 still significant in the horizontal slice (Figure 12d) at 10 m depth. This indicates that the
420 influence extent of the #2 mining area on the surface is still severe, which is confirmed by
421 the cracks on the surface of the village east of the study site.



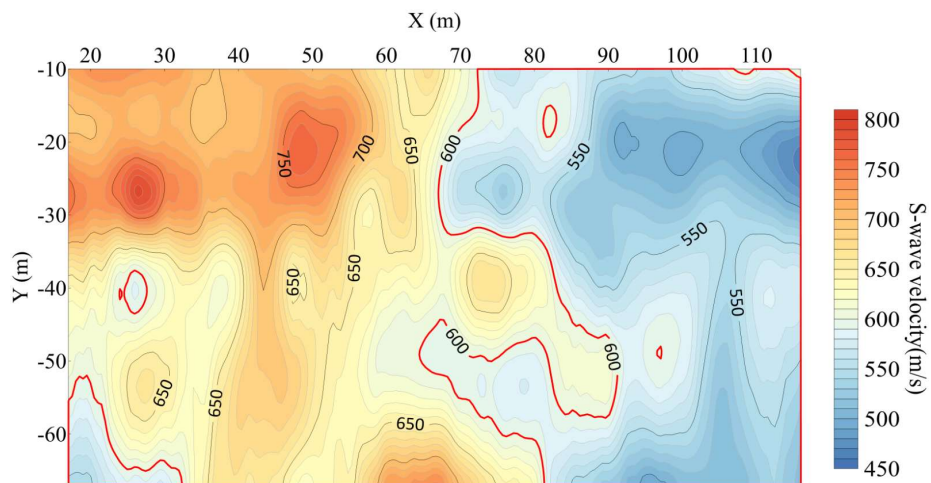
422

(a) Slice of 50 m depth



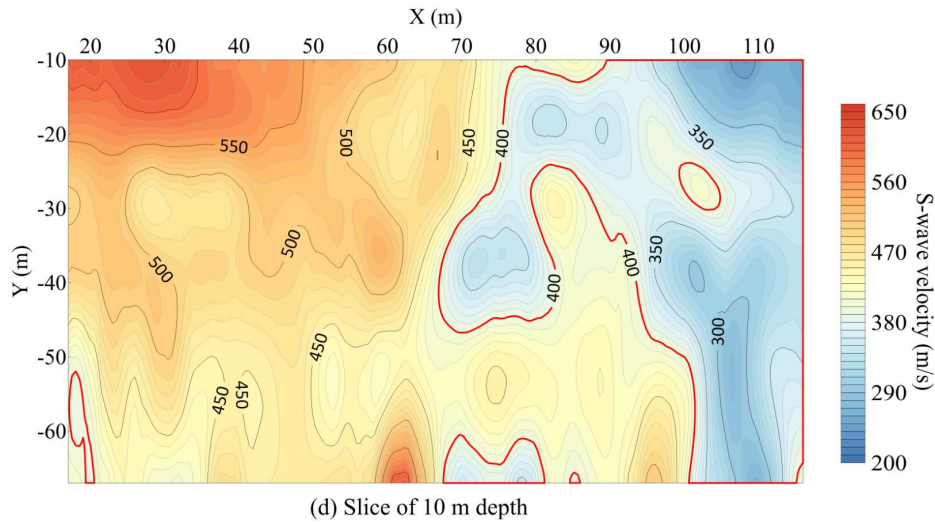
423

(b) Slice of 35 m depth



424

(c) Slice of 20 m depth



425

426 **Fig.12** Shear-wave horizontal slice of overburden427 **5. CONCLUSION**

428 a. The phase-shift method is improved by introducing a low-frequency focusing factor, and a
 429 low-frequency focusing phase-shift method is proposed. The procedure is based on the short
 430 receiver spread, which can significantly improve the focus of the dispersion energy at low-
 431 frequency side while extending the dispersive energy to lower frequencies. Applying this method
 432 to the real data, the receiver-spread length of the measured data used to calculate the dispersion
 433 energy is 35 m, which meets the 70 m detection depth of the target coal mined-out area.

434 b. The measured data is processed to obtain high-precision horizontal slice of shear wave
 435 along the coal seam and identified the boundaries of the mined-out areas, the locations of the
 436 security coal pillars. Based on the geometries exhibited by the security coal pillars and the
 437 mined-out areas, this site's leading coal mining direction is estimated to be approximately 23°
 438 NW. This coincides with the actual direction of 21° NW for the layout of the recovery face in the
 439 mining area of the study site. Furthermore, based on the locations and geometries of the security

440 coal pillars, two mined-out areas with one roadway are inferred, where the width of the roadway
441 is approximately 10 m.

442 c. After the coal seam is mined, the shear wave velocity of the overburden decreases and
443 shows low velocity characteristics. The horizontal slices of shear wave at different depths above
444 the coal seam indicate the influence extent by the coal mined-out areas obviously. The overall
445 trends of the low-velocity zone gradually decrease as the depth decreases. In this case, the extent
446 of the low-velocity zone is still significant in the horizontal slice at 10 m depth, which is
447 confirmed by the cracks on the surface of the village east of the study site.

448 d. The effectiveness of the low-frequency focused phase-shift method in improving the
449 lateral resolution of the MASW method and the feasibility of the MASW method for fine
450 detection of shallow coal mined-out area and overburden are confirmed. The low-frequency
451 focused phase-shift and MASW methods are shown to have good application prospects in
452 precisely detecting shallow coal mined-out area and overburden.

453 **DATA AVAILABILITY**

454 Data contained in this paper can be obtained by contacting the corresponding author.

455 **CONFLICTS OF INTEREST**

456 The authors declare that they have no known competing financial interests or personal
457 relationships that could have appeared to influence the work reported in this paper.

458 **FUNDING STATEMENT**

459 This work was supported by the National Key Research and Development Project [grant

460 number2018YFC0807803]; Nature Science Basic Research Plan in Shanxi Province of China [gr
461 ant number 2019JLM8]; and the Fundamental Research Funds for the Central Universities, CHD
462 [grant number 300102260203].

463

REFERENCES

464 Chang SL, Zhang ST, Li GS, Wei JS (2002) Application of multichannel transient Rayleigh
465 wave method on survey of goaf in coal mine. *Coal Geology of China* (3):71-73.

466 Chen CY, Bai CX, Song LL, Xie ZH (2010) Application of the multichannel transient Rayleigh
467 wave method to highway goaf detection. *Progress in Geophysics (in Chinese)* 25(2):701-
468 708.

469 Chen ZM, Luo X, Yin ZX, Li W (2021) Electrical method exploration technology in goaf of
470 Pingshuo mining area[J]. *Journal of Liaoning Technical University (Natural Science)*
471 40(2):112-119.

472 Cheng JL (2008) Study on geophysical field characteristics of mining-induced fracture rock mass
473 in mine and its applications. *Journal of China University of Mining & Technology* (06):877-
474 879.

475 Cheng JL, Pan DM, Li W, Liu SC, Wang YH, Jiang GQ (2010) Study on the detecting of hazard
476 abandoned workings by ground penetrating radar on strong electromagnetic interference
477 area[J]. *Journal of China Coal Society* 35(2):227-231.

478 Cheng JL, Yu SJ (2000) Simulation experiment on the response of resistivity to deformation and
479 failure of overburden. *Chinese J. Geophysics. (in Chinese)* (5):699-706.

480 Cheng JY, Sun HX, Zhao QB, Su DG (2008) The detection technology of excavated region in
481 coal mine and case study. *Journal of China Coal Society* (03):251-255.

- 482 Du WF, Peng SP, Zhu GW, Yang F (2014) Time-lapse geophysical technology-based study on
483 over burden strata changes induced by modern coal mining. *International Journal of Coal*
484 *Science & Technology* 1(2):184-191.
- 485 Fu TG (2014) Study on technology of comprehensive geophysical method exploration of mine
486 goaf and water accumulated area. *Coal Science and Technology* 42(8):90-94.
- 487 Li F, Cheng JL, Chen SJ, Kang QT, Li GG, Liu DM (2019) Fine detection of overburden strata
488 based on time lapse high density resistivity method. *Journal of Mining Science and*
489 *Technology* 4(1):1-7.
- 490 Li LY, Xue JJ, Zhao XX, Cao QH (2017) The exploration of mined-out areas by integrated
491 geophysical method. *Geophysical and Geochemical Exploration* 41(2):377-380.
- 492 Li W (2017) Optimization study of surface comprehensive geophysical detection methods of
493 coal mine goafs. *Coal Science and Technology* 45(1):194-199.
- 494 Li ZH (2012) Research on integrated geophysical exploration for railway survey in coal mine
495 goaf. *Geophysical and Geochemical Exploration* 36(S1):20-26.
- 496 Liu JH, Wang ZW, Zhu S, Weng AH, Xia AY (2005) The geophysical exploration about
497 exhausted area and sinking area in coal mine. *Journal of China Coal Society* (6):715-719.
- 498 Liu YZ, Wang ZD (1996) Data collection and processing system of transient surface wave
499 method and examples of its Application. *Geophysical and Geochemical Exploration* (1):28-
500 34.
- 501 Meng ZP, Zhang JC, Joachim T (2006) Relationship between physical and mechanical
502 parameters and acoustic wave velocity of coal measures rocks. *Chinese J. Geophys.* (in
503 Chinese) 49(5).1505-1510.

- 504 Mu Y (2018) Experimental study on response characteristics of transient electromagnetic method
505 in shallow gob. *Coal Science and Technology* 46(10):203-208.
- 506 Park CB, Miller RD, Xia JH (1999) Multichannel analysis of surface waves. *GEOPHYSICS*
507 64(3):800-808.
- 508 Park CB, Miller RD, Xia JH (1998) Imaging dispersion curves of surface waves on multichannel
509 record. *SEG Technical Program Expanded Abstracts* :1377-1380.
- 510 Rector J W, Pfeiffe J, Hodges S, Kingman J, Sprott E (2015) Tomographic imaging of surface
511 waves: a case study from the Phoenix Mine, Battle Mountain, Nevada. *Leading Edge*
512 34(11):1360-1364.
- 513 Rix GJ, Leipski EA (1991) Accuracy and resolution of surface wave inversion. *Recent*
514 *Advances in Instrumentation, Data Acquisition & Testing in Soil Dynamics*. ASCE.
- 515 Su C, Li MX, Wang P (2020) Optimized inversion of TEM and CSAMT detection in goaf water
516 accumulation area of shallow coal seam. *Coal Science and Technology* 48(6):177-183.
- 517 Virieux J (1984) SH-wave propagation in heterogeneous media: velocity-stress finite-difference
518 method. *Exploration Geophysics* 15(4):265.
- 519 Virieux J (1986) P-SV wave propagation in heterogeneous media : velocity-stress finite-
520 difference method. *GEOPHYSICS* 51(4):889-901.
- 521 Wang P, Cheng JY, Yao WH, Li MX, W Y (2019) Technology of detecting water-filled goaf
522 beside borehole using downhole transient electromagnetic method. *Journal of China Coal*
523 *Society* 44 (8):2502-2508.
- 524 Wang WS, Zhang B, Geng YL, Geng YL, Fan YL (2004) Application of high resolution seismic
525 and large energy rayleigh wave methods in goaf detection. *Coal Geology of China* (6):47-49.

- 526 Wang Z, Li GF, Zhou XJ, Hu SY, Li RF, Chen WK, Jiao PS, Li C, Li JB (2021) Key problems
527 and countermeasures of CBM development through surface boreholes in abandoned coal
528 mines of Shanxi Province. *Coal Geology & Exploration* 49(4):86-95.
- 529 Xia JH, Miller RD, Park CB (1999) Estimation of near-surface shear-wave velocity by inversion
530 of Rayleigh waves. *GEOPHYSICS* 64(3):691-700.
- 531 Xue GQ, Pan DM, Yu JC (2018) Review the applications of geophysical methods for mapping
532 coal-mine voids. *Progress in Geophysics (in Chinese)* 33(05):2187-2192.
- 533 Yan YF, Sun CY, Lin TF (2019) Mapping water-rich goaf utilizing microtremor exploration
534 method[C]. *SEG Technical Program Expanded Abstracts* :3136-3140.
- 535 Yan YW (2019) Research on high-frequency surface wave imaging technique for the shallow
536 subsurface. Changchun : Jinlin University.
- 537 Yang JM (2012) The application of high density method to the exploration of coalfield goaf.
538 *Geophysical and Geochemical Exploration* 36(S1):12-15.
- 539 Yang SA, Ning SN (2004) Research on Seismic Surveying Goafing of the Old Mine. *Coal*
540 *Geology of China* (1):47-50.
- 541 Yu ZQ, Sun MW, Wang ZR. Application of transient Rayleigh wave exploration to engineering
542 geological survey. *Coal Geology of China* (S1):62-68.
- 543 Yuan H, Liu JP, Jiang ZX (2021) 4D Seismic Characteristics in Coal Mine Gobs: A Case Study
544 from the Zhangji Coal Mine in Huainan Coalfield. *Geoscience* 35(04):1018-1023.
- 545 Yuan L, Jiang YD, Wang K, Zhao YX, Hao XJ, Xu C (2018) Precision exploitation and
546 utilization of closed/abandoned mine resources in China. *Journal of China Coal Society*
547 43(1):14-20.

- 548 Zhang PS, Liu SD, Wu RX, Cao Y (2009) Dynamic detection of overburden deformation and
549 failure in mining workface by 3d resistivity method. Chinese Journal of Rock Mechanics
550 and Engineering 28(9):1870-1875.
- 551 Zhang Z, Yin QZ (2021) Case study on the effects of seismic exploration beneath the goafs of
552 different ages. Coal Geology & Exploration 49(6):237–242.
- 553 Zhou F (2012) Experiment of influence of fractures on coal/rock acoustic velocity: with
554 Carboniferous seams of Qinshui basin as example. Coal Geology & Exploration 40(02):71-
555 74.